

Pores in Bilayer Membranes of Amphiphilic Molecules: Coarse-Grained Molecular Dynamics Simulations Compared with Simple Mesoscopic Models.

C. Loison,^{1,*} M. Mareschal,² and F. Schmid^{3,†}

¹*Max Planck Institut für Chemische Physik fester Stoffe,
Nöthnitzer Str. 40, D-01187 Dresden, Germany*

²*Centre Européen de Calcul Atomique et Moléculaire,
ENS Lyon, 46, Allée d'Italie, F-69007 Lyon, France*

³*Fakultät für Physik, Universität Bielefeld, Universitätsstraße 25, D-33615 Bielefeld, Germany*

(Dated: June 28, 2018)

We investigate pores in fluid membranes by molecular dynamics simulations of an amphiphile-solvent mixture, using a molecular coarse-grained model. The amphiphilic membranes self-assemble into a lamellar stack of amphiphilic bilayers separated by solvent layers. We focus on the particular case of tensionless membranes, in which pores spontaneously appear because of thermal fluctuations. Their spatial distribution is similar to that of a random set of repulsive hard discs. The size and shape distribution of individual pores can be described satisfactorily by a simple mesoscopic model, which accounts only for a pore independent core energy and a line tension penalty at the pore edges. In particular, the pores are not circular: their shapes are fractal and have the same characteristics as those of two dimensional ring polymers. Finally, we study the size-fluctuation dynamics of the pores, and compare the time evolution of their contour length to a random walk in a linear potential.

I. INTRODUCTION

Fluid lipid bilayers are the basic material of biological membranes. Pores in such bilayers play an important role in the diffusion of small molecules across biomembranes.^{1,2,3} In the last decade, the interest in pore formation in bilayer membranes has greatly increased with the development of electroporation – in this technique, an intense electric field is applied for a short time allowing bulky hydrophilic molecules to permeate through the lipid membranes of a cell or a vesicle. Additionally, the formation of pores in bilayers is supposed to be one key step of the fusion of membranes.^{4,5,6}

One difficulty in studying the pores experimentally is that they are usually not visible in optical microscopy. Yet, they have been investigated using indirect techniques such as permeation measurements with micropipettes (*e.g.* Ref. 7) or small angle neutron scattering.⁸ The mechanisms of permeation through a membrane obviously depend on the size and the life-time distributions of the pores. Such data are difficult to obtain experimentally because of the small life-time and the small dimensions of the pores (less than a millisecond and a few nanometers).^{9,10} Therefore, numerical calculations – either with molecular models^{11,12,13,14,15} or with density functional theories^{16,17} – have proven useful to study the local structure of defects in amphiphilic bilayers and lamellar phases.

Models for pores dynamics^{1,18,19,20} are often based on Glaser's model of pore formation.²¹ He distinguishes between three stages. In the first stage, the bilayer thickness fluctuates because of thermal fluctuations. Some hydrophobic tails happen to be exposed to the solvent. In the second stage, the solvent spans through the hydrophobic layer, creating a hydrophobic pore. If this pore expands, it becomes energetically favorable for the am-

phiphiles in the edge of the pore to reorient. Finally, in the third stage, the pore possesses a hydrophilic edge (see Fig. 1). The final hydrophilic pores carry an energy E

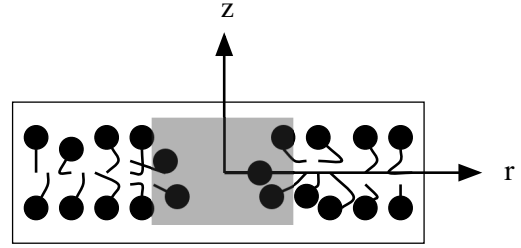


FIG. 1: Schematic cartoon of a hydrophilic pore in an amphiphilic bilayer (inspired by Ref. 21). The dark discs are the hydrophilic heads of the amphiphiles, the thin lines their hydrophobic tails. The solvent above/under the bilayer and in the pore is not represented. In the grey region, the structure of the bilayer is perturbed.

that depends on the contour length c and the area a of the pore. Lister²² suggested that

$$E = E_0 + \lambda c - \gamma a, \quad (1)$$

where E_0 is equivalent to a core energy, λ is the line tension of the pore edge, and γ the surface tension of the bilayer. In most cases, $\lambda > 0$ and $\gamma \geq 0$. According to Lister's model [Eq.(1)], for strictly positive surface tension, pores larger than a critical size are stable and the membrane may break. For tensionless membranes ($\gamma = 0$, the case we investigate here) the energy increases monotonously when the pore grows. Pores of any size are unstable, and the membrane is stable.

The aim of this article is to compare the results of molecular dynamics simulations to simple mesoscopic

models of pores in bilayers based on Eq. (1). The comparison has turned out to be fruitful for various models, and permits to bridge the gap between the descriptions at different length and time scales. Müller and coworkers¹² could show that pore formation in stretched bilayers composed of diblock-copolymers is effectively associated with a rearrangement of the amphiphilic molecules in the edge, as Glaser suggested. Recently, Talanquer et al.¹⁷ confirmed Eq. (1) using a density functional theory for amphiphilic bilayers.

Here we present a large scale study of spontaneously formed pores in a stack of tensionless bilayers. In stretched bilayers ($\gamma \neq 0$) the pore energy mainly depends on the pore area, but at zero surface tension ($\gamma = 0$), the relevant variable is the contour length c [see Eq. (1)]. In particular, we study systematically the shapes of pores, their spatial distribution within a bilayer, and their dynamical evolution.

The paper is organized as follows: in Sec. II we describe briefly the model of amphiphilic molecules and the molecular dynamics simulation methods which permit us to describe the lamellar phase in the $NPT\gamma = 0$ ensemble (for more details see Refs. 23,24). Then, the analysis of the molecular dynamics configurations is described. The results presented in Sec. III are divided into four parts. First, in Sec. III A, we present the density profiles around the pores. These show that we study hydrophilic pores, *i.e.* pores with a configurational rearrangement in the edge. In Sec. III B, the pore positions within a membrane are investigated. We conclude that the pores do not interact unless close to each other. In Sec. III C, we discuss the size and shape distribution of the pores and estimate the line tension λ associated to the configurational rearrangement in the pore edge. Finally, we trace the time evolution of individual pores. The results are described in Sec. III D, and interpreted with a simple stochastic model.²⁵ We summarize and conclude in Sec. IV.

II. MODEL AND METHODS

At the time-scale available to all-atoms molecular simulations (about 100 ns), the spontaneous formation of a pore in a lipid bilayer can be considered as a rare event. In fact, the formation of a pore in a DPPC bilayer was studied a few years ago with all-atom molecular dynamics¹⁴ of 256 lipids during 0.5 μ s, but this pore was observed in a far-from-equilibrium situation with a relatively small system. To explore the properties of thermally activated pores in equilibrium bilayers, we use a coarse-grained molecular model which describes relatively thin bilayers. In such simulations, many pores appear spontaneously during one simulation run.

A. Coarse-Grained Molecular Model

The model was presented in detail in a previous publication²³ and is based on well known similar models,^{26,27} therefore we recall here only its essential features. The bilayers are formed by amphiphilic molecules (molecules with a hydrophilic head-group and one hydrophobic tails) in a binary solution with solvent. All molecules are represented by one or several soft beads (for simplicity, all beads are taken to have the same mass m). The solvent is represented by single soft spheres (type s). The amphiphilic molecules are linear tetramers composed of two solvophobic beads (or “tail beads”, denoted t) and two solvophilic beads (or “head beads”, denoted h). The soft spheres of the amphiphilic h_2t_2 are connected by bonds.

Bonded beads are connected by a spring potential²⁶ independent of the bead-types:

$$U_{LJ-FENE}(r) = \quad (2)$$

$$\begin{cases} 4\epsilon \left[\left(\frac{\sigma}{r} \right)^{12} - \left(\frac{\sigma}{r} \right)^6 \right] - \left(\frac{\kappa T_b^2}{2\sigma^2} \right) \ln \left[1 - \left(\frac{r}{r_b} \right)^2 \right] & \text{if } r \leq r_b \\ \infty & \text{if } r_b \leq r \end{cases}$$

This potential comprises a Lennard-Jones type soft repulsive part dominating for $r \rightarrow 0$, and an attractive part diverging for $r \rightarrow r_b$ (the bond length is therefore confined between 0 and r_b). The length parameter σ is our unit of length and the energetic parameter ϵ our unit of energy. The bond parameters were fixed at $r_b = 2.0 \sigma$ and $\kappa = 7.0 \epsilon$.

Non-bonded beads interact with short ranged potentials of the general form

$$U_{LJ-cos}(r) = \quad (3)$$

$$\begin{cases} 4\epsilon \left[\left(\frac{\sigma}{r} \right)^{12} - \left(\frac{\sigma}{r} \right)^6 + \frac{1}{4} \right] - \phi & \text{if } r \leq 2^{1/6} \sigma \\ \frac{\phi}{2} [\cos(\alpha r^2 + \beta) - 1] & \text{if } 2^{1/6} \sigma \leq r \leq r_c \\ 0 & \text{if } r_c \leq r \end{cases}$$

This potential comprises again a Lennard-Jones type soft repulsive part, and a short-ranged attractive part. The range r_c of the potential is fixed at 1.5σ . The parameters α and β are fixed such that potentials and forces are continuous everywhere ($\alpha = \pi/r_c^2 - 2^{1/3}\sigma^2$ and $\beta = 2\pi - r_c^2\alpha$). The energetic parameter ϕ determines the depth of the potential; it depends on the types of the interacting beads. For pairs that “dislike” each other (ts and th), we choose $\phi = 0$ and so that the interaction is purely repulsive. For the sake of simplicity, for all the other pairs (ss , sh , hh , and tt), the potential depth ϕ of the pair interactions is the same ($\phi = 1.1 \epsilon$). For a fixed ϵ , the self-assembly is driven by the increase of ϕ only. The choice of $\phi = 1.1 \epsilon$ ensures that we simulate the liquid crystalline lamellar phase of the tetrameric amphiphiles.²³

In the following, lengths shall be given in units of σ , energies in units of ϵ and masses in units of m . This gives the time unit $\tau = (m\sigma^2/\epsilon)^{1/2}$. Typical orders of magnitude of our units are for example $\epsilon \sim 5 \cdot 10^{-21}$ J, $m \sim 10^{-25}$ kg, $\sigma \sim 5\text{\AA}$, and $\tau \sim 10^{-12}$ s. In this case, one solvent bead represents roughly three water molecules, and the tetrameric amphiphiles typically represent a symmetric neutral surfactant like C_6EO_3 . Such surfactants are much smaller than usual biological lipids. As a consequence, bilayers diluted in a large amount of solvent are not stable in our model (they separate into micelles). Thus, a quantitative comparison of our system with realistic lipid biomembranes is not our goal: we focus on the general properties of pores in bilayer membranes.

To study stable bilayer membranes, we simulated self-assembled L_α lamellar structures: a stack of amphiphile bilayers parallel to each other, separated by layers of solvent (see Fig. 2). At the temperature of the simulation, these bilayers are two dimensional fluids.^{23,24} In the present work, a smectic phase composed of fifteen bilayers containing several thousands of molecules each was simulated over $10^5 \tau$.

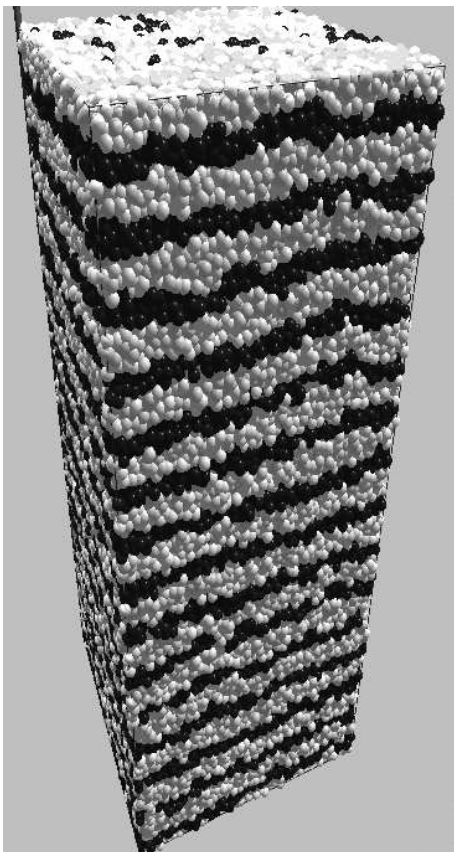


FIG. 2: Snapshot of the system (30 720 h_2t_2 and 30 720 solvent beads simulated in the NPT ensemble with $P/\epsilon = 2.9 \sigma^{-3}$, $k_B T = \epsilon$, and $\phi/\epsilon = 1.1$). The dark beads are solvophobic (type t), the light beads are solvophilic beads or solvent beads (type h or s).

B. Simulation Details

We have analyzed the same simulation runs as in a previous related article,²³ in which the lamellar L_α phase and its elastic properties are characterized in more detail. Here, we focus the analysis on the defects appearing in the bilayers due to thermal fluctuations. We have studied the model in the (NP_nP_tT) -ensemble (constant number of particles, constant pressure normal and tangential to the bilayers, and constant temperature) with molecular dynamics simulations. (N): The lamellar phase was studied at an amphiphile fraction of 80% of the beads (one solvent bead per h_2t_2). The system contained 30 720 tetramers and 30 720 solvent beads, which formed fifteen parallel bilayers of about two thousand molecules each (see Fig. 2).

(P): The normal and tangential pressure components P_n and P_t were kept constant using the extended Hamiltonian method of Andersen.^{28,29} The box shape is constrained to remain a rectangular parallelepiped. The box dimension perpendicular to the bilayer (L_z) and tangential to the bilayers (L_x, L_y) are coupled to two separated pistons. The thermal-averaged box dimensions were $L_x = L_y = 43.4 \pm 0.1 \sigma$ and $L_z = 31.9 \pm 0.1 \sigma$. We imposed the two pressure components separately rather than the total pressure $P = (P_n + 2P_t)/3$ because of technical reasons: the mechanical equilibrium is reached earlier, the orientation of the bilayers is stabilized, and the surface tension is controlled. Since we studied a bulk lamellar phase, we imposed an isotropic pressure ($P_n = P_t = P$). More details on the simulation algorithm and its parameters are given in Ref. 23. (T): The temperature was controlled by a stochastic Langevin thermostat that has been described earlier and applied to very similar models.^{26,27,30}

The dimensionless pressure and temperature were fixed at $P\sigma^3/\epsilon = 2.9$ and $k_B T/\epsilon = 1.0$. For the chosen dimensionless potential depth, $\phi/\epsilon = 1.1$, the density fluctuates around 0.85 beads per unit volume. With these typical parameters, lamellae form and order spontaneously. But this process requires at least 30 000 τ . We have therefore imposed the orientation of the lamellae in the initial configurations. They were constructed so, that fifteen bilayers separated by solvent layers were stacked in the z -direction. These configurations were then relaxed for 10 000 τ . During that time, the interlamellar distance adjusted to its equilibrium value, the shape of the flexible box changed accordingly, but the director remained basically aligned with the z -direction.

Data were then collected over $10^5 \tau$. We verified that the pressure tensor obtained at equilibrium was diagonal and isotropic, and that the surface tension $\gamma = \langle L_z(P_n - P_t) \rangle$ was negligible.²³ For the time independent analysis (Secs. III A, III B and III C), we have used 400 configurations separated by 250 τ . For the time dependent analysis (Sec. III D), we have used four series of 400 configurations separated by 1 τ . These series were separated by 10 000 τ .

C. Pore Detection and Analysis

Generally, several types of point defects exist in smectic phases. A highly aligned L_α phases may contain pores in the bilayers, but also necks or passages between two bilayers.^{31,32} Any of those defects changes the topology of the lamellar phase: pores in the bilayers connect two neighboring solvent layers, fusion between neighboring bilayers connect the bilayer matrices, and passages connect both neighboring solvent layers and neighboring bilayers. One possibility to detect a defect, and to distinguish between these defects is to analyze the topology of the lamellar phase.^{13,32} Using a cluster-algorithm on the simulated lamellar phase,²⁴ we observed that in our model L_α phase, necks and passages appear very rarely (in less than 1% of the configurations). So we can focus on the pores in the bilayers.

Figure 3 shows a representative snapshot of the tail-beads of one membrane. On the snapshot, five pores are

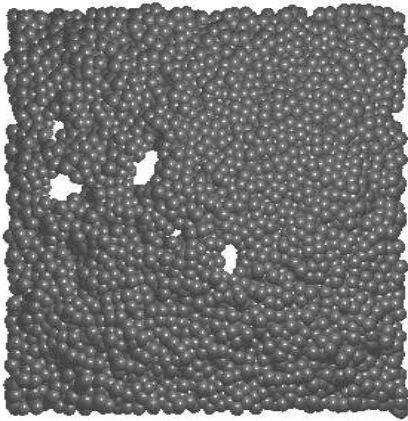


FIG. 3: Snapshot of the head-beads of one bilayer (top view).

clearly present.

For a systematic analysis, we defined a pore as a region of the inner part of the bilayer where relatively few tail-beads are present (*i.e.* the relative density of tail beads is less than a given threshold). The n th bilayer is defined by its position $h_n(x, y)$ and its thickness $t_n(x, y)$ (Monge representation).³³ In practice, only discrete values of x and y were considered ($x = n_x L_x / N_x$ and $y = n_y L_y / N_y$ where $n_{x,y}$ are integer values, $N_x = N_y = 32$, and $L_x = L_y \sim 43 \sigma$). Therefore, all the observables are measured on a two dimensional grid of 32×32 “plaquettes” of area $d_x \times d_y$ where $d_x = L_x / N_x$ and $d_y = L_y / N_y$. As the dimensions of the simulation box fluctuate, the mesh size also fluctuates: $dx = dy \sim 1.3 \pm 0.05 \sigma$. In the following, the notation “plaquette” indicates that area are expressed in units of the plaquette area and the lengths in units of the mesh size.

The analysis is divided into two steps (see Appendix A for more details): First, we have determined the local

positions and thickness of the membranes in every configuration from the relative densities of solvophobic beads $\rho_{tail}(x, y, z)$. For each point (x, y) , the relative density of tail beads $\rho_{tail}(x, y, z)$ oscillates as a function of z , with one maximum per bilayers. The position $h_n(x, y)$ and thickness $t_n(x, y)$ of a given membrane were determined as the mean and the difference of the two z values where $\rho_{tail}(x, y, z)$ equals a threshold value ($\rho_0 \sim 0.7$) around the appropriate maximum.

Second, the positions (x, y) where the thickness of the membrane n is zero or undefined are attributed to pores. We call them “pore-positions”. For each membrane, the pore-positions $\{x_i, y_i\}_n^{pp}$ are assembled into two dimensional clusters, the “pore-clusters”. Two pore-positions belong to the same pore-cluster if they share at least one vortex of the two-dimensional $N_x \times N_y$ grid.

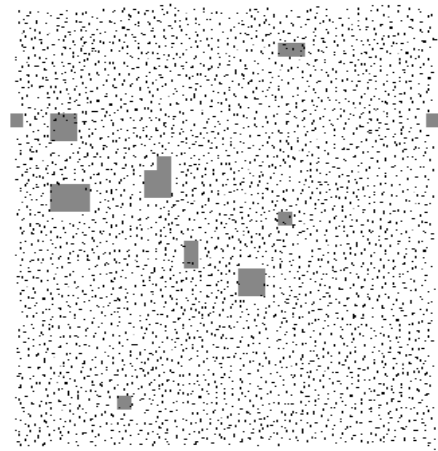


FIG. 4: Result of the pore analysis on the membrane depicted in Fig. 3. The single isolated square in the bottom left of the image is of the area of a single plaquette.

The result of such an analysis is represented on Fig. 4. In this figure, the dots represent the centers of the tail-beads belonging to the membrane (seen in Fig. 3). Each pore-position is represented by a grey square. The resulting grey patches are the pore-clusters. Each pore visible in Fig. 3 appears under the form of a pore-cluster. But additional small pores-clusters that were not visible on the snapshot also appear in the analysis. It seems that some tail-beads (black dots) are still present in those pores. In practice, it was difficult to decide whether these small pore-clusters are noise, fluctuations of the bilayer thickness, or hydrophobic pores. In particular, no minimum life-time was found for these pores of minimum size. Therefore, the pore-clusters composed of one plaquette only were disregarded in the following analysis (unless noted otherwise).

For each of the pore-clusters, which we call only “pores” for simplicity, the mean position \mathbf{r}_{cm} , the matrix of gyration $g^{\alpha\beta}$, the area a and the contour length c were calculated. Again, these observables are defined for clusters of pixels on the two dimensional $N_x \times N_y$ grid.

The mean position is calculated via

$$\mathbf{r}_{cm} = \frac{1}{n_{pp}} \sum_{i=1}^{n_{pp}} \mathbf{r}_i, \quad (4)$$

where the sum runs over the n_{pp} pore-positions of the pore cluster, and \mathbf{r}_i is the position of the pore-position number i .

The gyration matrix is given by

$$g^{\alpha\beta} = g_0 + \frac{1}{n_{pp}} \sum_{i=1}^{n_{pp}} (\mathbf{r}_i - \mathbf{r}_{cm})^\alpha (\mathbf{r}_i - \mathbf{r}_{cm})^\beta, \quad (5)$$

where α and β denotes axes of the grid, and g_0 the gyration matrix of one plaquette, which we approximated by one fourth the identity matrix (in plaquette area).

III. SIMULATION RESULTS

In each bilayer of area $L_x L_y \sim 1850 \sigma^2$, the average number of pores is 9.9 ± 1.3 . Their total area corresponds to approximately 1% of the projected area of the bilayer. Among these ten pores, 5.7 ± 1.0 pores on average have the minimum size of one plaquette (with an area of about $1.7 \sigma^2$).

A. Composition Profiles through the Pores

Figure 5 shows the composition in head, tail and solvent beads around the center of relatively small pores (of area two to four plaquettes). They are represented in the cylindrical coordinates with the center of the pore as origin: $\rho_{tail}(\mathbf{r}, z)$, $\rho_{head}(\mathbf{r}, z)$, $\rho_{solvent}(\mathbf{r}, z)$, where the z -axis is perpendicular to the bilayers (see Fig. 1). We averaged over the directions of \mathbf{r} in the plane of the bilayer and over the two sides of the bilayers for the values $+z$ and $-z$, so the composition is represented as a function of $|r|$ and $|z|$.

Far from the pore centers, at distances $r \geq 4\sigma$, the typical bilayer structure is found. The tails are segregated inside the bilayer ($z \leq 2\sigma$). For intermediate z (around 2σ), the head-beads shield the tail-beads from the solvent. The solvent is concentrated near the mid-bilayer plane ($z = 3.2\sigma$). As defined by our detection algorithm, the pore ($r \rightarrow 0, z \leq 3\sigma$) is characterized by the absence of tail-beads inside the bilayer. The head and solvent distributions show that the interior of the pore is occupied by head-beads rather than solvent-beads. Even inside the pore, the head-beads shield the tail-beads from the solvent. We conclude that pores with an area a larger than two plaquettes are of “hydrophilic type”. As expected, the same observation is made for larger pores (data not shown). To summarize, the amphiphiles of the pore edge are reoriented in our model, even for the small pores ($a = 2, 3, 4$ plaquettes). Notably, such a reorientation was also observed by Müller and co-workers in the

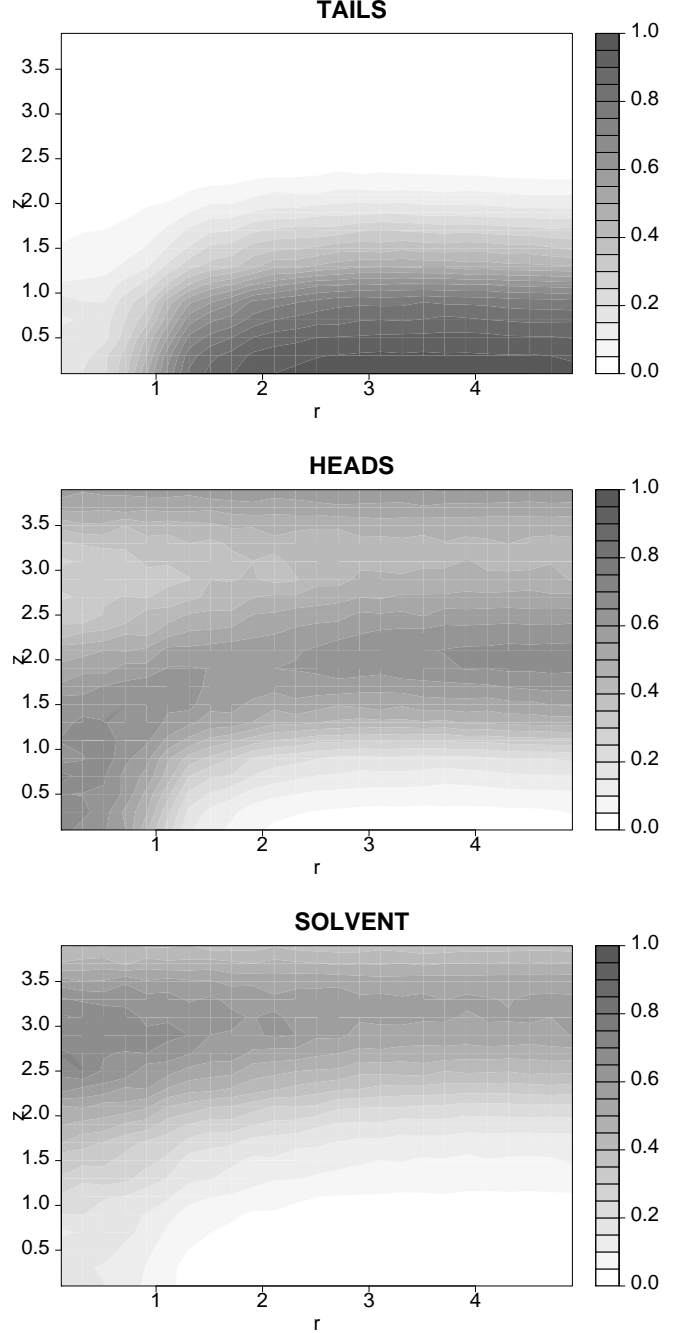


FIG. 5: Composition profiles around the centers of pores with areas between two and four plaquettes (length unit: σ). Note that the inter-bilayer distance is 6.4σ , so the mid-bilayer plane (between a bilayer and its next neighbor) is at $z = 3.2 \sigma$

pore edges of amphiphilic bilayer of block-copolymers.¹² As a consequence, it is reasonable to use Eq. (1) to interpret our simulation data: the energy of a pore is expected to increase with the contour length of the pore.

B. Positions Correlations of the Pores

About four pores of area larger or equal to two plaquettes are present in each simulated membrane of area $L_x \times L_y \sim 43 \times 43 \sigma^2$. Do these pores interact? A priori, they are at least subject to hard core repulsion, because two pores cannot overlap (overlapping pores would be considered as a single pore). In this section, we try to detect whether there exist additional soft interactions between the pores.

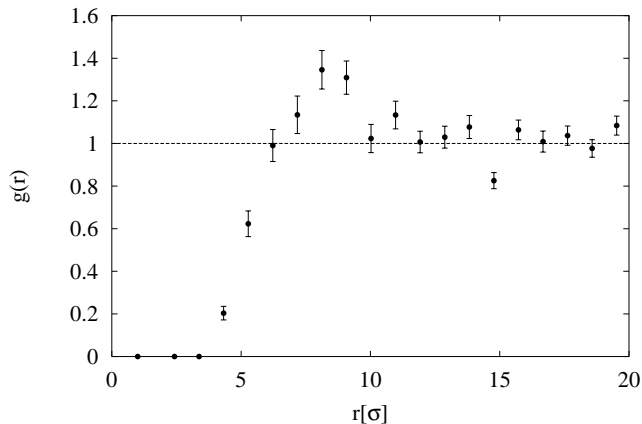


FIG. 6: Spatial pair correlation function of the center of the pores. As we neglected the correlations between the distributions of pores in different membranes of the same configuration, the errorbars are under-estimated.

The most straightforward approach to this problem is to look for spatial pair correlations between the pores (see Fig. 6). In this analysis, we have taken into account all the pores, even the smallest ones ($a = 1$ plaquette). Despite the noise of the data, two tendencies are clear. At large distances, say about $r \geq 10 \sigma$, no correlation is observed. At small distances ($r \leq 5 \sigma$), the short-range repulsion between the pores is reflected by a depletion in the pair correlation function. At intermediate distances ($r \sim 8 \sigma$), the data suggest a slight positive correlation, *i.e.* the probability that pores open up seems to be slightly increased in the vicinity of other pores. The statistics is however not sufficient to justify a conclusive statement.

An alternative, complementary method of analyzing spatial distributions of patterns in physical systems has been proposed by Mecke and others^{34,35,36,37,38,39}: the evaluation of Minkowski functionals. Minkowski functionals have been used in various areas of mathematics, chemistry and physics to analyze high-order correlations of spatial distributions. The present analysis is similar to the one developed and applied by Mecke, Jacobs and co-workers^{34,40} to study the spatial distribution of defects in a thin film of polymers. The analysis can be decomposed into two steps (see Fig. 7). First, on each of the N points of the distribution, a square of size l is

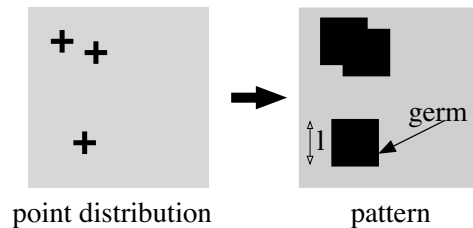


FIG. 7: Principle of the Minkowski analysis (see text for more explanations).

fixed (the germ).⁴¹ These N germs form a two dimensional image, the pattern. In two dimensions, the three dimensionless Minkowski functionals $m_{0,1,2}$ of a pattern are proportional to its surface A , contour length C and Euler characteristic χ ³⁶: $m_0 = A/A_t$ where A_t the total area of the surface, $m_1 = C/\sqrt{A_t N}$, where N is the number of points in the distribution, and $m_2 = \chi/N$. We used an algorithm described by Milchielsen³⁷ to calculate the Minkowski functionals of a digitalized pattern (without periodic boundary conditions). Finally, the dimensionless Minkowski functionals are represented as a function of the dimensionless coverage factor $x = l^2 N/A_t$ where l^2 is the area of the square germ.

Figure 8 shows the three Minkowski functionals obtained from about 1000 pore distributions containing *exactly* six pores of area larger than two plaquettes (symbols). We compare these results with three reference distributions (curves).

The first reference is a random distribution of fixed germs on an infinite surface (Poisson), for which the Minkowski functionals are known analytically³⁶:

$$m_0(x) = 1 - \exp(-x) \quad (6a)$$

$$m_1(x) = 4\sqrt{x} \exp(-x) \quad (6b)$$

$$m_2(x) = (1 - x) \exp(-x) \quad (6c)$$

The pore distributions obviously differ from a Poisson distribution on an infinite surface. We attribute the discrepancy to two effects: finite size effects, and repulsion effects. The former are due to the finite size of our quadratic grid, and to the finite area of the membranes. Explicit expressions for the Minkowsky functionals in a finite “observation window” on an infinite surface are given in Ref. 34. Here, we have additional boundary effects because only germs inside the window contribute to the pattern. Therefore, we have calculated the expected finite size effects numerically.

Two reference distributions on a finite grid of 32×32 pixels were considered. In the first one, which we call “finite random” (FR) distribution, a fixed number of points was distributed randomly. The second one, denoted “finite self-avoiding” (FSA) takes into account the hard-core repulsion between pores, *i.e.* pores may not touch or overlap (see Appendix). As Figure 8 shows, the differences between FR and FSA distributions are relatively

small, but observable. We present here the results for bilayers containing six pores, but the same conclusions are drawn for different densities (the data are not shown; as expected, the influence of self-avoidance increases with the density of points).

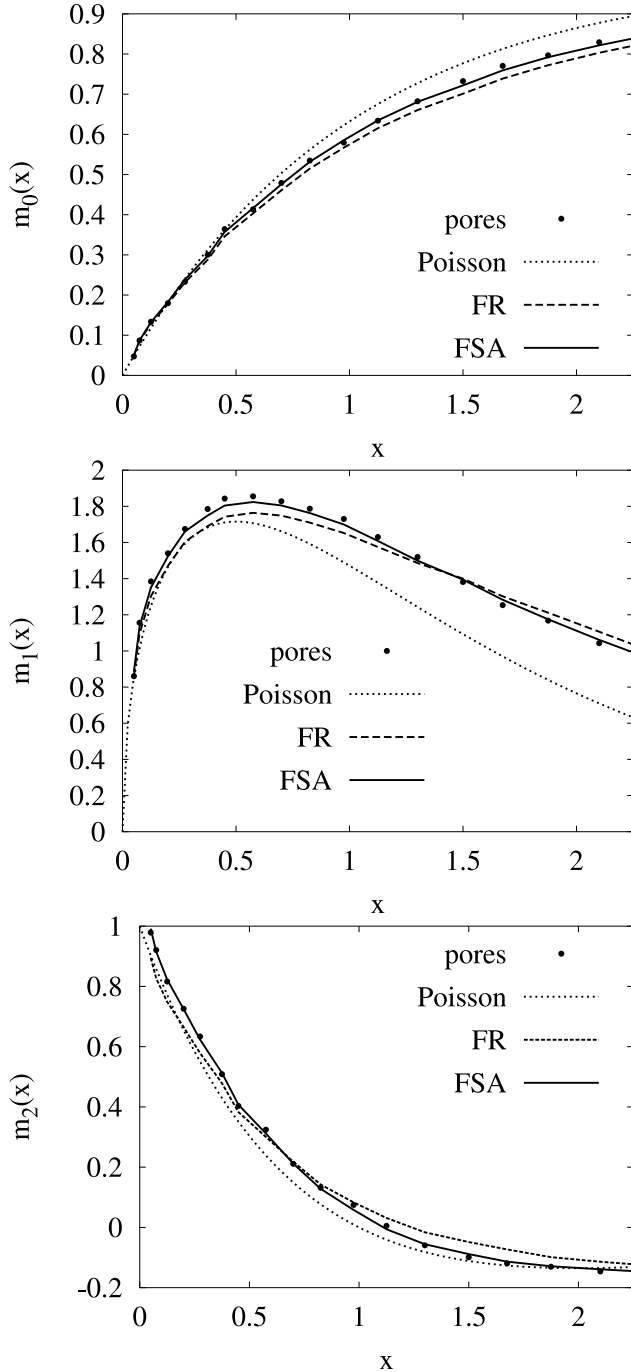


FIG. 8: Dimensionless Minkowski functional as a function of the dimensionless coverage factor (6 points on a 32×32 grid). “Poisson” corresponds to Eq. 6, FR to the numerical results obtained with 1000 Finite Random distributions, and FSA to the numerical results obtained with 1000 Finite Self-Avoiding distributions (see text and Appendix).

The results obtained with the pore distributions of the simulations are closer to those obtained with the FSA distributions. Therefore, both finite size effects and self-avoidance are observable in the Minkowski analysis, and these two effects seems to be sufficient to account for the data.

To conclude, the pores are not distributed randomly in the membrane. The spatial distribution of pores is compatible with a simple model, in which the pores interact only through a hard-core repulsion. Additional soft interactions between pores may be present, but these do not influence the overall pore distribution significantly.

We have also studied the correlations between pores in different membranes. Not surprisingly, a small correlation is observed, *i.e.* the probability that a pore opens up on top of another pore is slightly increased. But we did not explore this effect throughout.

C. Size and Shape of the Pores

In the following the area of the pores, their contour length and their radius of gyration are analyzed. In this section, all pores have been taken into account, even the smallest ones ($a = 1$ plaquette).

As shown in Section III B, the spatial distribution of the pore within a membrane were in good agreement with the hypothesis that the pore interact only via a hard-core repulsion. In the following, we consider the pores as independent. Within this hypothesis, the contour length distribution $P(c)$ of the pores can be compared to the Boltzmann factor $g(c) \exp[-E(c)/(k_B T)]$, where $E(c)$ is the energy to create a single pore of contour length c and $g(c)$ is the degeneracy. We calculated $g(c)$ for the particular quadratic grid of our analysis (see Table I).

The ratio $P(c)/g(c)$ is shown in Fig. 9 in a linear-log plot. The approximated energy of pore formation $-\ln[P(c)/g(c)]$ is well described by a linear function. Fitting the model $E(c) = E_0 + \lambda c$ to the data yields the line tension $\lambda = 0.7 \pm 0.1 k_B T \cdot \sigma^{-1}$. This value is approximately $5 \cdot 10^{-12} J \cdot m^{-1}$, which agrees reasonably with the values calculated by May⁴² for the excess free energy of the packing rearrangement of amphiphiles in the edge. Previous results^{9,12,43} report line tensions in the range of $10^{-11} J \cdot m^{-1}$ to $3 \cdot 10^{-11} J \cdot m^{-1}$, *i.e.* larger than the present value. In these references, the line tension includes also the excess free energy necessary to transfer the amphiphiles from a reservoir to the edge of pore (the chemical potential of the amphiphiles in the grey region of Fig. 1). This contribution (typically $10^{-11} J \cdot m^{-1}$) is proportional to the surface tension of the bilayer^{12,42} and vanishes in the present case.

In brief, the size distributions computed with the simulations are compatible with the usual mesoscopic model of pores energetics and permit to compute the approximate line tension of the pore edge.

The shape of the pores have been studied with the two-dimensional gyration matrix of the pore-clusters [see

| | | | | | | | |
|------|---|---|---|----|-----|-----|------|
| c | 4 | 6 | 8 | 10 | 12 | 14 | 16 |
| g(c) | 1 | 2 | 9 | 36 | 168 | 715 | 2000 |

TABLE I: Degeneracy of the contour length c of clusters of pixels connected by at least one vortex. As explained in Section II C, a pore is defined as a cluster of pixels connected by at least one vortex. In our calculations, the directions $-x$, x , $-y$ and y are distinguishable. We neglect the finite size of the grid (a square of 32 plaquettes), therefore all positions of the pores on the grid are considered as equivalent. Because of the high cost of such calculations, the value are exact only up to $c = 14$. The value for $c = 16$ is an under-estimate.

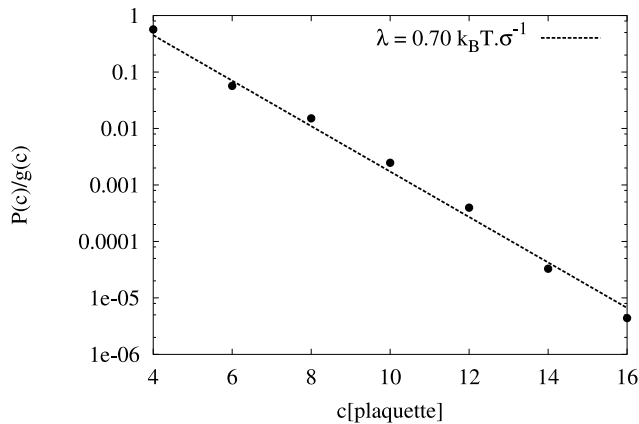


FIG. 9: Probability distribution function of the contour of the pores $P(c)$, divided by the degeneracy of the contour length $g(c)$ (linear-log plot).

Eq. (5)]. The two (positive) eigenvalues of the gyration matrix are denoted ρ_1^2 and ρ_2^2 . The sum of the eigenvalues $R_g^2 = \rho_1^2 + \rho_2^2$ is the square of the radius of gyration of the pore, and the relative difference $|\rho_1^2 - \rho_2^2|/R_g^2$, its asymmetry - it is zero for a circular pore and tends towards one when the pore is elongated in one direction. Figure 10 represents the radius of gyration of the pores as a function of their area. As expected, the square of the radius of gyration increases linearly with the area of the pores. A least-square linear fit yields $R_g^2 \sim 0.17a + 0.29$ (both in units of σ^2). The proportionality factor (0.17) is slightly larger than the proportionality factor obtained for a homogeneous disc ($[2\pi]^{-1} \sim 0.15$).

As illustrated in Fig. 11, the asymmetry of the pores does not vary significantly with the size of the pores, except for the smallest pores, whose asymmetry is imposed by the finite mesh size of the grid.

This suggests that only one length-scale is sufficient to describe the pore dimension. Notably, the average asymmetry is not zero (0.35 ± 0.05). In fact, since the bilayers are flaccid, there is no reason why the pores should be circular. Müller and co-workers⁶ emphasized the importance of the asymmetric shape of pores on the mechanism of fusion between two parallel bilayer membranes.

The pore shape can also be studied via the correla-

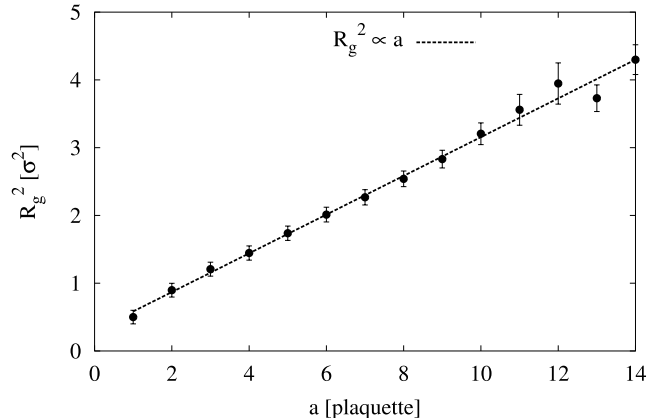


FIG. 10: Square of the radius of gyration of the pores, as a function of their area.

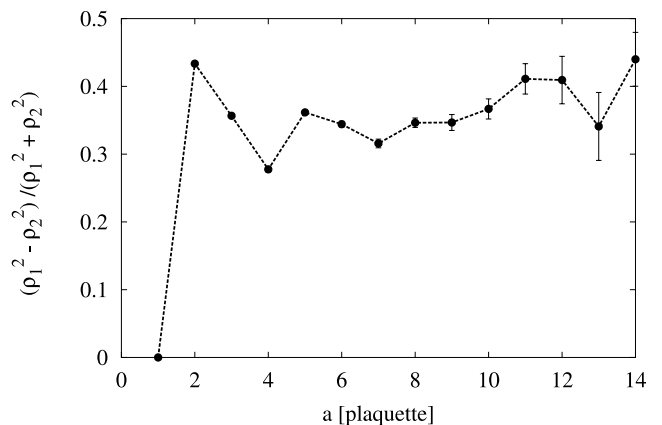


FIG. 11: Asymmetry of the pores as function of their area.

tion between the area and the contour length. Figure 12 shows the pore area a as a function of the contour length c in a log-log representation. The simulation data are well represented by the equation

$$a \propto c^{3/2}. \quad (7)$$

Such a relationship is consistent with the results obtained by Shillcock *et al.*¹⁹ for their study of the proliferation of pores in fluid membranes. As Shillcock *et al.* remark, two dimensional flaccid vesicles⁴⁴ and two-dimensional ring polymers⁴⁵ show the same behavior as pores in flaccid membranes. These different objects may be modeled as closed, self-avoiding, planar random-walks whose energy depends only on the number of steps. As a consequence, the correlation between the area a and contour length c observed in our simulations [see Eq. (7)] is consistent with the simple model of the pore energy given by Eq. (1) (with $\gamma = 0$). We emphasize that the present study and Ref. 19 are not using the same types of model. Shillcock *et al.* simulated pores in membranes at a meso-

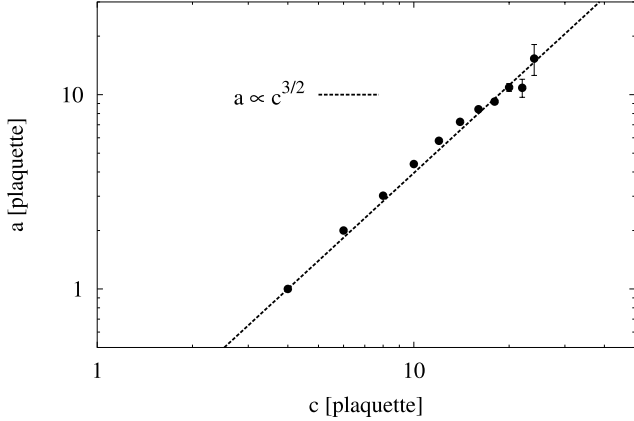


FIG. 12: Area of the pores as a function of their contour length (log-log plot).

scopic length-scale, with Monte Carlo simulations based on Eq. (1), whereas in our simulations, Eq. (1) emerges from the molecular model.

D. Dynamics of size fluctuations

In the previous section, we have shown that static properties of the pores (size and shape distributions) are in very good accordance with Eq. (1). In the following section, we investigate the dynamics of the pore size by comparing the simulation results to a simple stochastic model based on Eq.(1). First we determine the time-scale of the pore dynamics. Second, we present the stochastic model and we check the relevance of the assumptions of the model for our simulation results. Finally, the “shrinking-time” distribution of the pores of the model is fitted to the simulation results and the resulting parameters are briefly discussed.

To characterize the short-time dynamics of the contour length c , we have measured the number of jumps $\Omega(c, dc)$ from c to $c + dc$ during one time interval (Δt) . The probability $P(c, dc)$, that a jump with the initial contour length c has the amplitude dc is then defined as

$$P(c, dc) = \frac{\Omega(c, dc)}{\sum_{dc} \Omega(c, dc)}. \quad (8)$$

An appropriate numerical value for Δt is slightly lower than the typical time that a pore needs to change its size. The time-scale of pore dynamics is expected to be of the same order of magnitude as that of configurational rearrangements of the amphiphiles, *i. e.*, 10^{-12} s to 10^{-11} s (close to 1τ). To estimate this time-scale, we studied the correlation time of average quantities like the total contour length, and the total area of pore per bilayer (see Fig. 13). As expected, the correlation times range around 2τ . Given this first estimate of the time-scale dynamics,

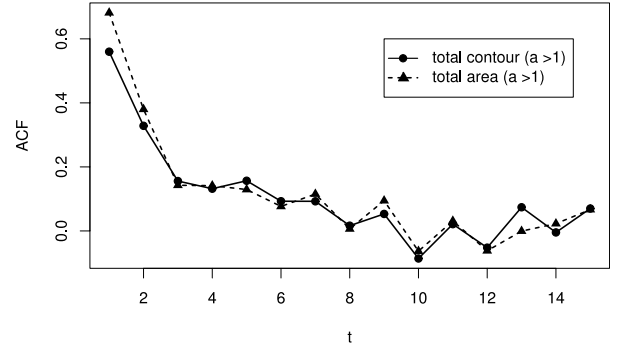


FIG. 13: Autocorrelation functions of the total areas and contour lengths as a function of time (time unit: τ). The pores of area $a = 1$ plaque are not included in the analysis.

we studied the time-evolution of individual pores every 1τ .

We compare our results with a simple stochastic model that has been solved analytically: a random walk in a linear potential (RW-LP model).²⁵ The RW-LP model describes a random walk in a semi-infinite one-dimensional space with discrete states labeled $n = 0, 1, 2, \dots, \infty$. For the interpretation of our simulation results, the variable $n(t)$ represents one half of the contour length $c(t)$. The time evolution consist of discrete jumps of amplitude $|dn| = 1$, at an average rate W . The probability to hop towards the upper neighbor ($n \rightarrow n + 1$) is $p^+ = (1 - b)/2$. In the other direction ($n \rightarrow n - 1$), it is $p^- = (1 + b)/2$. The bias $0 \leq b \leq 1$ measures the tendency to walk towards $n = 0$, where the walker dies (absorbing boundary). In our interpretation, the parameter b is proportional the line tension of the pores. For this model, the probability $Q(n, t|n_0)$ that a walker starting from the state n_0 reaches the state $n < n_0$ for the first time after having walked during the time t is²⁵

$$Q(n, t|n_0) = \frac{n_0 - n}{t} \left(\frac{1+b}{1-b} \right)^{\frac{n_0 - n}{2}} e^{-Wt} I_{n_0 - n}(Wt\sqrt{1 - b^2}), \quad (9)$$

where I_ν , ($\nu \geq 1$) is the modified Bessel Function of the first kind, and W and b are the two parameters of the model. In Eq. (9), the time t is the time needed by the variable n to shrink from $n_0 > n$ to n , so we call it “shrinking time” and Q “shrinking-time distribution”.

Of course, the simulation data are more complicated than the RW-LP model. (i) The model supposes that within the time W^{-1} , only jumps of amplitude $|dc| = 2$ occur. In the simulations, its is obviously not the case. Nevertheless, the jump probability $P(c, dc)$ decreases when the amplitude of the jump $|dc|$ increases (see Fig. 14). For our choice of $\Delta t = 1\tau$, 80% of the jumps with $dc \neq 0$ correspond to the amplitude $|dc| = 2$. One might expect that if the time of observation is small enough, we should observe exclusively jumps of the small-

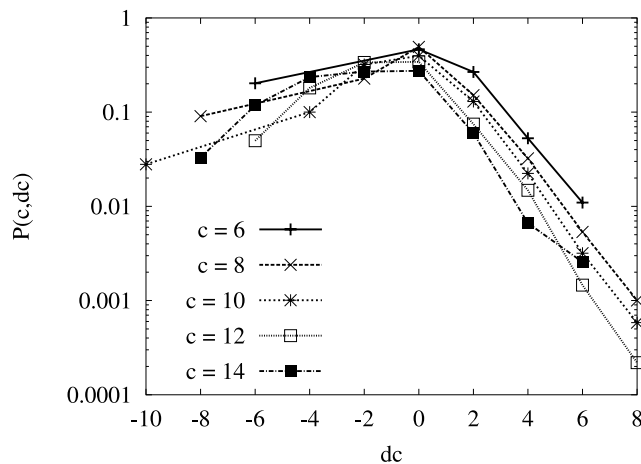


FIG. 14: Probability of jumps from c to $c+dc$ as a function of dc for possible values of the initial contour length c (linear-log scale).

est amplitude. We find however that even for the observation time $\Delta t = 0.1 \tau$, some jumps with large amplitude $|dc| \geq 6$ appear. The frequency of jumps is thus broadly distributed.

(ii) The model supposes that the effective potential $(-\ln P(c))$ is a linear function of c . In the simulation, it is not linear because of a large entropic contribution to the free energy (data not shown here, see Ref 24). Nevertheless, the effective potential increases with the pore size; In Fig. 14 the energetic bias is clearly seen: for a given amplitude $|dc|$, the probabilities to jump with $dc < 0$ are much larger than for $dc > 0$.

(iii) The model does not describe the complex behavior of small pores, especially the dynamics of hydrophilic pore formation.

After discussing the assumptions of the RW-LP model, we show that this stochastic model, yet simple, fit the simulation data. We have measured $Q(n, t | n_0)$ for the simulations using $n_0 = 5$ and $n = 4$. This choice permits to restrict ourselves to large pores ($c \geq 8$); therefore, we do not describe the dynamics of the formation of the pores, but only of their shape and size fluctuations. As expected from Eq. (9), other choices of $\{n, n_0\}$ with $n_0 - n = 1$ and $n_0 \geq 5$ give very similar results. Fig. 15 shows the comparison between the simulation data (symbols) and Eq. (9) with the parameters $b = 0.2$ and $W = 0.5 \tau^{-1}$ (curve). Despite the simplicity of the model, the agreement is very good and the fitted parameters are reasonable: The value of the frequency $W = 0.5 \tau^{-1}$ is consistent with the previously estimated correlation time of the size fluctuation (2τ). The value of the bias $b = 0.2$ is also consistent with the slope s of the free energy $-\ln P(c)$ as a function of c ($s = 0.1 k_B T$ per plaquette⁴⁶). To conclude, not only the statics, but also the dynamics of the pore size is in good agreement with Lister's model.

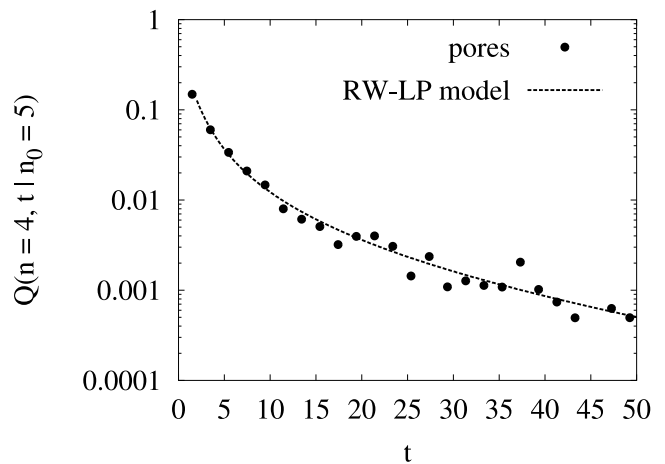


FIG. 15: Probability that a pore of contour $c = 10$ reaches the contour $c = 8$ for the first time after having fluctuated during the time t (observation time $\Delta t = 1 \tau$), in a linear-log plot. The line represents Eq. (9) with $n_0 = 5$, $n = 4$, $W = 0.5 \tau^{-1}$, and $b = 0.2$. We had to renormalize the pore distribution to fit it to Eq. (9), because it was normalized on the range $t \in [2, 450]$ whereas Eq. (9) is normalized on the range $t \in [0, \infty]$.

IV. CONCLUSIONS

We have investigated a bulk lamellar phase in an amphiphilic system by molecular dynamics simulations, using a phenomenological off-lattice model of a binary amphiphile-solvent mixture. The system was studied in the $(NP_n P_t T)$ -ensemble using an extended Hamiltonian which ensured that the pressure in the system was isotropic. Therefore, the membranes had no surface tension. At high amphiphile concentration, (80% bead percent of amphiphiles), the amphiphilic molecules self-assemble into a lamellar phase, *i.e.*, a stack of bilayers. The pores appearing spontaneously in the bilayers were studied.

The molecular structure of the pores shows that the amphiphiles situated in the rim of the pore reorient: the hydrophilic heads shield the hydrophobic tails from the solvent.

The mean effective free energy of a single pore was computed from the distribution of the contour-lengths c of the pores. Taking into account the entropic effect of shape fluctuation, we could fit the simple model $E(c) = E_0 + \lambda c$ to the simulation data, and estimate the line tension λ of the pores.

Without surface tension, the pores are not circular. The relationship between the area a of the pores and their contour-length c is well described by the law $a \propto c^{2/3}$. This relationship was found for other two-dimensional objects, whose energy depends only on their contour length (models of flaccid vesicles⁴⁴ and of self-avoiding ring-polymers).⁴⁷ The analogy between our simulation results and these “random-walk” models suggest that in our analysis, the “bending energy” of the pore edge is

negligible.

Finally, the shrinking-time distribution $Q(n, t|n_0)$ decreases relatively slowly with the time t (it can be fitted, for example, by the power law \mathcal{T}^{-2}). The long tail of this probability distribution indicates the existence of particularly stable pores. Presumably, these correspond to pores that have grown very large before shrinking again. Despite its simplicity, the model of one-dimensional random walk in a linear potential (RW-LP)²⁵ reproduces nicely the distribution of the shrinking times observed for the pores.

To summarize, we have studied in great detail the pore statics and dynamics in a molecular model, and found that our data are in excellent agreement with the predictions of a mesoscopic line tension theory $E(c) = E_0 + \lambda c$. Our results establish that such simple phenomenological models do indeed describe many aspects of real pores in self-assembled membranes. We have demonstrate that for a relatively simple, coarse-grained model, which does however treat the particles on a microscopic level. Thus we believe that our conclusion will also hold for more realistic models, as long as long-range interactions can be neglected.

Acknowledgments

We thank Kurt Kremer, Peter Reimann, Ralf Eichhorn and Ralf Everaers for fruitful discussions. We acknowledge the Max Planck Gesellschaft for computation time at the computing center of Garching.

APPENDIX A: ALGORITHM TO DETECT AND ANALYZE THE PORES.

This appendix describes how we determined the local positions of membranes in the lamellar stack and the position of the pores in the membranes.

1. The space is divided into $N_x N_y N_z$ cells of size (dx, dy, dz) with $N_x = N_y = 32$ and $N_z \sim 92$. For a density of 0.85 particle per volume unit, $dx = dy \simeq 1.3 \sigma$ and $dz \simeq 1.0 \sigma$. The size of cells may slightly vary from one configuration to another because the dimensions of the box dimensions vary.
2. The relative density of tail beads in each cell is calculated as the ratio $\rho_{tail}(x, y, z) = N_{tail}(x, y, z)/N_{tot}(x, y, z)$ where $N_{tail}(x, y, z)$ is the number of tail beads in the cell (x, y, z) and $N_{tot}(x, y, z)$ the total number of particles in this same cell.
3. The membranes are defined as the space where the relative density of tail beads is higher than a threshold ($\rho_{tail}(x, y, z) > \rho_0$). The choice of the threshold depends on the mesh size in x and y directions ($dx = L_x/N_x$ and $dy = L_y/N_y$). Typically, we used

ρ_0 from 0.65 to 0.75 (80 % of the maximum relative density of tail beads; values for $dx = dy \sim 1.3\sigma$).

4. The cells that belong to membranes are associated into three dimensional clusters: Two membrane-cells that share at least one vortex are attributed to the same membrane-cluster. Each membrane-cluster defines a membrane. This algorithm identifies membranes even if they have holes. In the presence of necks between adjacent membranes (local fusion), additional steps have to be taken in order to find the necks until one membrane-cluster per membrane is found (not detailed here).
5. For each membrane n and each position (x, y) , the two heights $h_n^{min}(x, y)$ and $h_n^{max}(x, y)$ where the density $\rho_{tail}(x, y, z)$ equals the threshold ρ_0 are estimated by a linear extrapolation. The mean position and the thickness are then defined by

$$\begin{aligned} h_n(x, y) &= \frac{1}{2} [h_n^{max}(x, y) + h_n^{min}(x, y)] \\ t_n(x, y) &= \frac{1}{2} [h_n^{max}(x, y) - h_n^{min}(x, y)] \end{aligned} \quad (A1)$$

6. The positions (x, y) where the thickness of the membrane n is zero or undefined are considered as “pore-positions”. For each membrane, an ensemble of pore-positions $\{x_i, y_i\}_n^{pp}$ is obtained.

APPENDIX B: FSA DISTRIBUTIONS

We sketch here the principle of our construction of “finite self-avoiding” (FSA) distribution of NPOINTS points of size `size` on a grid of booleans `template` of dimensions `NX*NY`. Each boolean `template[i, j]` can take the value `FREE` or `OCCUPIED`. A schematic algorithm can be written in the following way (not in a real programming language, and without any control about the feasibility of the task !):

```
function ConstructFSA(NX,NY,NPOINTS,size)
  n = 0;
  Initialize(template,NX,NY,FREE)
  while(n<NPOINTS)
    xn = NX*random()
    yn = NY*random()
    if(template[xn,yn] == FREE)
      x[n] = xn
      y[n] = yn
      Set_occupied(template,xn,yn,size)
      n = n+1
    end_if
  end_while
end_function
```

where `random()` is a random number generator whose output ranges between 0 and 1. At the end of the loop (it is ever reached !), the vectors `x` and `y` contains the

coordinates of the points of the distribution. The function `Set_occupied(template,i,j,size)` attributes the label `OCCUPIED` to all the sites of the `template` around the site `(i,j)`.

```
function Set_occupied(template,i,j,size)
  a = integer((size+1)/2);
  for(di= -a ; di <= a; di ++)
```

```
    for(dj= - a; dj <= a ; dj ++)
      template[i+di,j+dj] = OCCUPIED
end_function
```

We have used the following parameters : $NX = NY = 32$, $NPOINTS = 6$, $size = 3$, and calculated the mean value of the Minkowski functionals over 1000 distributions.

* Electronic address: loison@cpfs.mpg.de

† Electronic address: schmid@physik.uni-bielefeld.de

- ¹ S. A. Freeman, M. A. Wang, and J. C. Weaver, *Biophys. J.* **67**, 42 (1994).
- ² R. Lawaczeck, Ber. Benenges. Phys. Chem. **92**, 961 (1988).
- ³ S. A. Paula, A. G. Volkov, A. N. V. Hoeck, T. H. Haines, and D. W. Deamer, *Biophys. J.* **70**, 339 (1996).
- ⁴ S. A. Safran, T. L. Kuhl, and J. N. Israelachvili, *Biophys. J.* **81**, 859 (2001).
- ⁵ G. Hed and S. A. Safran, *Biophys. J.* **85**, 381 (2003).
- ⁶ M. Müller, K. Katsov, and M. Schick, *J. Chem. Phys.* **116**, 2342 (2002).
- ⁷ K. Olbrich, W. Rawicz, D. Needham, and E. Evans, *Biophys. J.* **79**, 321 (2000).
- ⁸ M. C. Holmes, A. M. Smith, and M. S. Leaver, *J. Phys. France II* **3**, 1357 (1993).
- ⁹ D. V. Zhelev and D. Needham, *Biochim. Biophys. Acta* **1147**, 89 (1993).
- ¹⁰ K. C. Melikov, V. A. Frolov, A. Shcherbakov, A. V. Samsonov, Y. A. Chizmadzhev, and L. V. Chernomordik, *Biophys. J.* **80**, 1829 (2001).
- ¹¹ S. J. Marrink, F. Jähnig, and H. J. C. Berendsen, *Biophys. J.* **71**, 632 (1996).
- ¹² M. Müller and M. Schick, *J. Chem. Phys.* **105**, 8282 (1996).
- ¹³ R. Holyst and W. T. Gozdz, *J. Chem. Phys.* **106**, 4773 (1997).
- ¹⁴ S. J. Marrink, E. Lindahl, O. Edholm, and A. E. Mark, *J. Amer. Chem. Soc.* **123**, 8638 (2001).
- ¹⁵ D. Zahn and J. Brickmann, *Chem. Phys. Lett.* **352**, 441 (02).
- ¹⁶ R. R. Netz and M. Schick, *Phys. Rev. E* **53**, 3875 (1996).
- ¹⁷ V. Talanquer and D. W. Oxtoby, *J. Chem. Phys.* **118**, 872 (2003).
- ¹⁸ W. Sung and P. J. Park, *Biophys. J.* **73**, 1797 (1997).
- ¹⁹ J. C. Shillcock and U. Seifert, *Biophys. J.* **74**, 1754 (1998).
- ²⁰ J. C. Shillcock and D. H. Boal, *Biophys. J.* **71**, 317 (1996).
- ²¹ R. W. Glaser, S. Leikin, L. V. Chernomordik, V. F. Pastushenko, and A. I. Sokirko, *Biochim. Biophys. Acta* **940**, 275 (1988).
- ²² J. D. Lister, *Physics Letters* **53A**, 193 (1975).
- ²³ C. Loison, M. Mareschal, K. Kremer, and F. Schmid, *J. Chem. Phys.* **119**, 13138 (2003).
- ²⁴ C. Loison, Ph.D. thesis, Ecole Normale Supérieure de Lyon and Bielefeld University, 2003.
- ²⁵ M. Khanta and V. Balakrishnan, *Pramana* **21**, 111 (1983).
- ²⁶ K. Kremer and G. Grest, *J. Chem. Phys.* **92**, 5057 (1990).

- ²⁷ T. Soddemann, B. Dünweg, and K. Kremer, *Eur. Phys. J. E* **6**, 409 (2001).
- ²⁸ H. C. Andersen, *J. Chem. Phys.* **72**, 2384 (1980).
- ²⁹ M. Parrinello and A. Rahman, *Phys. Rev. Lett.* **45**, 1196 (1980).
- ³⁰ A. Kolb and B. Dünweg, *J. Chem. Phys.* **111**, 4453 (1999).
- ³¹ Y. Bouligand, *Liq. Cryst.* **26**, 501 (1999).
- ³² D. Constantin and P. Oswald, *Phys. Rev. Lett.* **85**, 4297 (2000).
- ³³ S. A. Safran, *Statistical thermodynamics of surfaces, interfaces, and membranes* (Addison-Wesley Publishing Company, , 1994).
- ³⁴ K. R. Mecke, *Inter. J. Mod. Phys. B* **12**, 861 (1998).
- ³⁵ U. Brodatzki and K. R. Mecke, *Comput. Phys. Comm.* **147**, 218 (2002).
- ³⁶ K. R. Mecke, in *Lecture Notes in Physics 554: The Art of Analyzing and Modeling Spatial Structures and Pattern Formation*, edited by K. R. Mecke and D. Stoyan (Springer, Berlin, Heidelberg, New York, 2000), pp. 111–184.
- ³⁷ K. Milchielsen and H. D. Raedt, *Physics Reports* **347**, 462 (2001).
- ³⁸ *The Art of Analyzing and Modeling Spatial Structures and Pattern Formation*, Vol. 554 of *Lecture Notes in Physics*, edited by K. R. Mecke and D. Stoyan (Springer Verlag, Berlin, Heidelberg, New York, 2000).
- ³⁹ *Morphology of Condensed Matter - Physics and Geometry of Spatially Complex Systems*, Vol. 600 of *Lecture Notes in Physics*, edited by K. R. Mecke and D. Stoyan (Springer Verlag, Berlin, Heidelberg, New York, 2002).
- ⁴⁰ K. Jacobs, S. Herminghaus, and K. R. Mecke, *Langmuir* **14**, 965 (1998).
- ⁴¹ The difference between our analysis and the one of Ref. 40 is that our germs are squares, whereas theirs are disks.
- ⁴² S. May, *Eur. Phys. J. E* **3**, 37 (2000).
- ⁴³ J. D. Moroz and P. Nelson, *Biophys. J.* **72**, 2211 (1997).
- ⁴⁴ S. Leibler, R. Singh, and M. Fisher, *Phys. Rev. Lett.* **59**, 1989 (1987).
- ⁴⁵ J. P. Flory, *Principle of Polymer Chemistry* (Cornell University Press, Cornell, 1953).
- ⁴⁶ To correlate the measurement, we use the (very crude) approximation $(1-b)/(1+b) \sim \exp(-4s/k_B T)$ or $1-2b \sim 1-4s/k_B T$.
- ⁴⁷ M. Bishop and C. Saltiel, *J. Chem. Phys.* **88**, 3976 (1988).